



Experimental and computational failure analysis of hydrogen embrittled steel cords in a reinforced thermoplastic composite pipe

M. Elkhodibia ^a, G. Mubarak ^b, I. Gadala ^{c,d}, I. Barsoum ^{a,e,*}, A. AlFantazi ^b,
A. Al Tamimi ^f

^a Department of Mechanical and Nuclear Engineering, Khalifa University, Abu Dhabi, 127788, United Arab Emirates

^b Department of Chemical and Petroleum Engineering, Khalifa University, Abu Dhabi, 127788, United Arab Emirates

^c Center for Applied Research, NOVA Chemicals Corporation, 2928 16 St NE, Calgary, AB T2E 7K7, Canada

^d Department of Materials Engineering, The University of British Columbia, 6350 Stores Rd, Vancouver, BC V6T 1Z4, Canada

^e Advanced Digital and Additive Manufacturing Center, Khalifa University, Abu Dhabi, 127788, United Arab Emirates

^f Abu Dhabi National Oil Company (ADNOC), Abu Dhabi, 898, United Arab Emirates



ARTICLE INFO

Keywords:

Failure analysis
Corrosion
Finite element analysis
Ductile damage
Hydrogen embrittlement

ABOUT

Reinforced thermoplastic pipes (RTPs) have attracted considerable attention lately in the oil and gas sector as potential alternative to carbon steel pipes. However, some RTP systems have been experiencing failures as a result of deficient design and inadequate operation practices. This study presents a comprehensive assessment of the failure of a steel-reinforced flexible thermoplastic layered pipe in a sour environment characterized by hydrogen sulfide (H_2S) exposure. Utilizing scanning electron microscopy (SEM) and electron dispersive spectroscopy (EDS), the investigation conclusively attributes the failure of the RTP to hydrogen embrittlement of the carbon steel cords and wires in the reinforcement layer. Finite element models at both meso-scale and full RTP scale were developed, incorporating a novel damage initiation and propagation criterion for failure prediction of embrittled and non-embrittled (e.g. ductile) reinforcement steel cords. The numerical models consistently predicted a reduced burst pressures of the hydrogen embrittled case of the RTP, with a close match with field observations. They also predicted failure modes that closely matched the SEM findings, hence highlighting the unsuitability of the existing steel cords in RTPs for use in sour service environments. Additionally, the presence of moisture in the annular space was identified as an exacerbating factor. This investigation provides important insights for the future design and operation of RTPs susceptible to hydrogen embrittlement, paving the way for improved structural integrity and safety measures. Further research avenues may involve modeling hydrogen diffusion in the thermoplastic layers, simulating the movement of moisture in the annulus through the capillary effect, and incorporating fracture toughness degradation for a more thorough understanding of the interplay between mechanical and environmental factors in the hydrogen embrittlement of steel-reinforced RTP composite pipes.

1. Introduction

Pipeline systems play a critical role in various industries, including oil and gas transportation, where they are responsible for the safe and efficient conveyance of fluids over long distances [1–3]. The escalating severity of safety risks and environmental concerns

* Corresponding author at: Department of Mechanical and Nuclear Engineering, Khalifa University, Abu Dhabi, 127788, United Arab Emirates.
E-mail address: imad.barsoum@ku.ac.ae (I. Barsoum).

<https://doi.org/10.1016/j.engfailanal.2024.107962>

Received 10 November 2023; Received in revised form 26 December 2023; Accepted 2 January 2024

Available online 5 January 2024

1350-6307/© 2024 The Author(s). Published by Elsevier Ltd. This is an open access article under the CC BY license (<http://creativecommons.org/licenses/by/4.0/>).

arising from the corrosion and leakage of carbon steel pipelines in oil and gas gathering and transportation systems has emerged as a significant technical obstacle impeding the advancement of oil and gas exploration and development [4–8].

To address the corrosion issues associated with carbon steel pipelines in these corrosive environments, non-metallic and inert composite pipes have emerged as an alternative, offering advantages such as corrosion resistance, lightweight, increased specific strength, reduced maintenance requirements, enhanced durability, spool-ability and flexibility in design and installation [2,9–12]. Various types of non-metallic composite pipes are available, including Aramid reinforced thermoplastic pipes (RTPs) [13–15], steel-reinforced plastic composite pipes [16,17], and glass fiber-reinforced plastic pipes [18]. Within this range of non-metallic or inert composite pipes, steel wire-reinforced high-density polyethylene (HDPE) composite pipe stands out with its notable characteristics. With its large diameter, manufacturability and excellent transmission efficiency, this type of RTP has gained extensive application in the oil and gas industry. Because of their intrinsic corrosion resistance, RTPs outperform their typical carbon steel counterpart in this regard. This resistance can significantly extend the lifespan of the pipelines, reduces maintenance requirements, and ensure the integrity of the transported media [19,20]. These composite pipes are typically constructed with a dual-layer HDPE, comprising an inner and an outer layer, incorporating a plastic barrier layer. This multi-layered configuration of HDPE imparts exceptional chemical resistance and flexibility, leveraging the inherent benefits of HDPE. To enhance their ability to withstand higher pressures, steel cords are introduced as a reinforcement layer, which are typically galvanized to improve corrosion resistance. Notwithstanding, the utilization of such non-metallic pipes has effectively addressed the issue of corrosion commonly associated with conventional metal pipes, certain challenges related to the migration of the corrosive medium to the load-bearing steel wires can lead to performance degradation and localized failures [21]. Instances such as swelling [22], defects in the environmentally protective polymer layers [23–25], and gas permeation through the inner HDPE layer [26–28] have been reported. Over time, carbon-dioxide (CO_2) and hydrogen sulfide (H_2S) gradually permeate the HDPE layers [29]. In the presence of moisture, the permeation of CO_2 and H_2S can potentially lead to sweet [30] or sour [31] corrosion and subsequent embrittlement of the steel wires in the reinforcement layer.

As demand for these non-metallic pipes increases, there has been a growing interest in understanding their mechanical behavior. Numerous studies have examined their mechanical properties when subjected to internal pressure loading. Finite element modeling (FEM) has been commonly used in these studies to provide a clearer understanding of their overall behavior. Few studies have focused on simulating the behavior of steel RTPs via FEM using linear elastic material considerations [32–36]. However, the mechanical response of these RTPs can be non-linear, and consequently the incorporation of their nonlinear behavior can be necessary [37]. To this end, Shi et al. [38] considered the elastic–plastic behavior of the constituents, and analyzed the influence of the nonlinear properties of materials in a steel reinforced RTP on its burst pressure prediction. Furthermore, Shi et al. [16] incorporated plasticity, large deflection, and large strain capabilities in their FEM to study the behavior of a steel reinforced RTP under combined internal pressure and bending moment at various temperatures. Their study showed a relative error between the FEM results and test data ranging from –3.09% to 6.56%.

The aim of the current study is to explore the failure mechanisms of a RTP, as shown in Fig. 1(a), consisting of a HDPE jacket and liner and reinforced with galvanized high-strength AISI 1020 braided skeleton steel cords. The work combines experimental and computational evaluation to understand and pinpoint the cause of failure, and provides an in-depth assessment of the failure of RTPs under embrittlement conditions.

2. Background of failure

The failed RTP under consideration is a FlexCord Linepipe, which is a braided steel wire reinforced thermoplastic pipe with a cross-sectional schematic shown in Fig. 1(a). The RTP comprises a thermoplastic liner (inner HDPE liner), a thermoplastic jacket (outer HDPE jacket), two layers of braided galvanized steel cords wound between the liner and jacket, and an HDPE barrier layer fitted between the steel cord windings. The design of the steel cords is illustrated in Fig. 1(b), wherein each galvanized steel cord comprises a total of 19 wires. The arrangement consists of one central wire, with six wires encircling it and an additional twelve wires surrounding the initial six wires.

The failure event pertains to an occurrence of a burst in a RTP injection header handling produced water, as depicted in Fig. 2(a). The RTP system is responsible for transporting produced water originating from oil wells during crude oil extraction. This water often carries hydrocarbons and various chemical constituents from the reservoir. The leak was identified when the injection discharge pressure fell below the designated threshold. The failed segment measures 1311 m in total length. The pipeline has an outer diameter (OD) of 128 mm and an inner diameter (ID) of 99 mm. The daily production rate through the compromised section stands at approximately 650 cubic meters. The process stream maintains an average temperature of around 35 °C. During normal operation, the pipe operates within a range of 9.65 to 10.34 MPa for the affected segment, with a maximum pressure of 10.55 MPa recorded. The pipe's maximum operating pressure is rated at 13.79 MPa.

3. Experimental methodology

3.1. Visual examination

A systematic examination of the failed RTP is carried out to identify the root causes of its failure. The RTP's design and dimensions are analyzed, followed by a visual inspection of the sample and an evaluation of its external and internal surfaces. Key physical attributes, including the length of the failed RTP, the presence of a field crimp fitting coupling, and the location of failure, are

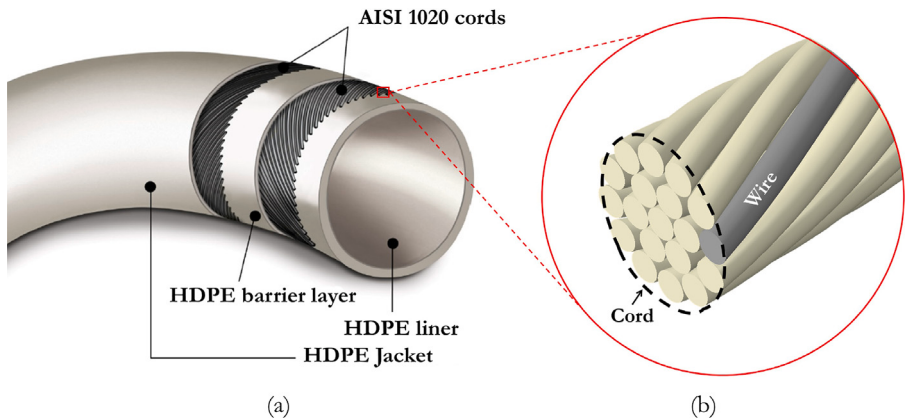


Fig. 1. Schematic illustration of (a) the RTP design, and (b) the assembly of a galvanized steel cord with its 19 wires [39].



Fig. 2. (a) RTP section with failed steel reinforcement wires and HDPE jacket, (b) crimp-fit sleeve with vent hole and exposed reinforcement wire ends, and (c) burst location in RTP.

assessed. Signs of damage on the external surface, such as discoloration, adhesion of soil or corrosion deposits, and scratches, are examined. The crimp fitting sleeve is removed, enabling inspection of the HDPE jacket, the steel crimp fitting, and the detection of Denso paste or rust staining. During the dissection of the failed sample, the failure location and characteristics, including the fracture surface of the outer jacket, are evaluated. The outer and inner layers of steel cords, along with the barrier layer, are examined for any signs of damage, separation, or corrosion. Finally, the internal steel mandrel, seals, and inner liner are inspected for visible defects or signs of degradation.

3.2. Chemical spot testing

Chemical spot tests are performed to assess the internal steel cords and the steel mandrel's outer surface. These tests are preceded by a solvent cleaning process to remove hydrocarbon contamination. Observations of the spots are made under a stereo microscope and are conducted on the internal steel cords at various locations. This is carried out both near and far from the failure site, aiming to detect sulphides indicative of H_2S corrosion and carbonates signifying CO_2 corrosion. In addition, chloride spot tests are executed on both the internal steel cords and on the steel mandrel's outer surface to identify the presence of chlorides indicating potential leakage of the produced water beyond the o-ring seals.

3.3. SEM and EDS

The reinforcement steel cords underwent examination using a scanning electron microscope (SEM) and followed by energy-dispersive X-ray spectroscopy (EDS) to analyze their chemical composition, microstructure and damage micro-mechanism. Prior to SEM examination, some of the failed steel cords were subjected to ultrasonic cleaning in a hot Alconox solution. Sample preparation involved mounting the wire cord samples on a plate, and the SEM examination focused on two aspects: fracture surfaces and wire cord sides, as shown in Fig. 3. Fracture surfaces were examined to identify different fracture modes, differentiating between ductile and brittle fractures. The wire cord sides were examined for evidence of corrosion and the composition of surface deposits.

3.4. Hardness testing

Hardness measurements were conducted on the surface of the wire cross-sections using Vickers hardness scale (HV). Micro-hardness readings were obtained using a Shimadzu Hardness Tester Type M with a load of 500 g (HV500 g). Vickers hardness readings were converted to Rockwell C hardness in accordance with the ASTM A370 [40]. For the HDPE components, Shore D hardness measurements were performed on the external surface of both the outer HDPE jacket and the inner HDPE liner at room temperature. The hardness was measured using a Shore D durometer in accordance with ASTM D 2240 [41] to identify any material deficiency in the HDPE layers that could have contributed to the failure.

4. Experimental results

4.1. Visual examination

During the overall visual examination, several key observations were made. The location of the perforation and subsequent burst was identified approximately 0.17 m from the end of the crimp-fit sleeve, as shown in Fig. 2(a). As seen in Fig. 2(a), the crimp-fit sleeve contained mold indentations and a vent hole, visible in Fig. 2(b). It is noteworthy that these mold indentations align consistently with the manufacturer's specifications, as verified through length measurements. Discoloration, adhesion of soil and corrosion deposits, and linear scratches were observed on the external surface of the RTP, likely resulting from contact with the pipe chute during installation and operation underground. The most significant external damage, aside from the failure location, were gouges and circumferential markings suggesting rotational movement between the pipe and its surroundings during installation or operation. None of these damages fully penetrated the outer HDPE jacket, and hence met the acceptance criteria outlined by the manufacturer.

After removing the crimp-fit sleeve, a cut out of the HDPE jacket at the RTP burst location was visually examined, as shown in 2(a) and (c), revealing rupture in the HDPE jacket and rupture of reinforcement wires. Remnants of Denso paste, which is commonly used for moisture displacement and corrosion inhibition, and discolouration indicated the presence of water and prior corrosion as seen in Fig. 2(b). Exposed cords and wires at the pipe bend suggested incomplete sealing by the Denso paste during installation and operation. Signs of water ingress and corrosion degradation were observed at the vent hole area of the crimp-fit sleeve. The failure was found to occur within the outer jacket, rupturing in the winding direction of the steel cords in the outer reinforcement layer, as shown in Fig. 2(a). The twisted nature of the RTP at the failure location indicated a failure induced by internal pressure. Furthermore, the fracture surface of the outer jacket exhibited significant plastic deformation, characteristic of ductile fractures commonly observed in materials such as HDPE, as expected. The outer HDPE jacket contained steel wire cords, covered by a barrier layer with helical lines corresponding to the inner wire cords' winding direction. The barrier layer exhibited ductile fracture characteristics, and no mechanical damage was found except at the failure site. Both the barrier layer and outer jacket failed in the same location along the winding direction of the steel cords. The intact steel cords indicated separation rather than breakage. Overall, the findings align with failure due to internal pressure.

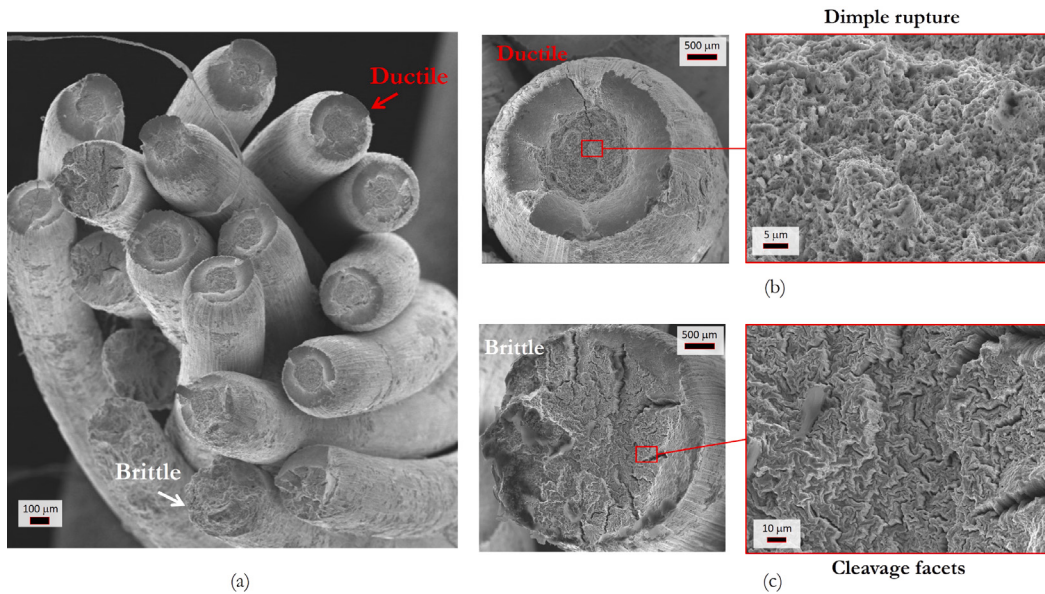


Fig. 3. SEM image of (a) a failed cord with multiple wires, revealing (b) ductile and (c) brittle failure.

4.2. Chemical spot testing

Chemical spot testing was carried out on the internal steel cords and the outer surface of the steel mandrel to identify potential corrosion-related compounds and leakage of internal media, respectively.

The spot tests on the internal steel cords indicated the presence of sulphides, suggesting H₂S corrosion. This finding aligns with the presence of H₂S in the internal media, which likely diffused through the inner liner to reach the steel cords [42]. Furthermore, the tests revealed positive results for carbonates, indicating CO₂ corrosion at the steel cords. This could be attributed to the presence of CO₂ or atmospheric corrosion of the galvanized coating, resulting in zinc carbonate formation. However, it should be noted that the absence of chlorides in the spot test results does not necessarily indicate their absence, as chlorides can be easily washed away. In contrast, the chemical spot tests conducted on the outer surface of the steel mandrel showed negative results for chlorides, as seen in Fig. 2(d). This suggests that the O-rings effectively sealed the inner liner, preventing significant leakage of chloride-rich produced water through these seals.

4.3. SEM and EDS

The examination of fracture surfaces using SEM revealed insights into the fracture modes observed in the steel cords and their wires. Both ductile and brittle fracture modes were identified, as seen in Fig. 3(a). Ductile fractures exhibited distinct characteristics such as cup-and-cone shapes, necking and presence of shear lips, as shown in Fig. 3(b), with micro-void nucleation, growth and coalescence as the governing ductile failure micro-mechanisms. Conversely, brittle fracture is observed on the outer steel wires of the cord, exhibiting limited plastic deformation with the appearance of a flat fracture surface, as shown in Fig. 3(c), indicating that cleavage facet formation being the governing brittle failure micro-mechanism.

The SEM examination of the steel cord and its wire's surfaces revealed evidence of corrosion and surface deposits. The corrosion products and deposits appeared as multilayered structures, indicating the involvement of multiple corrosion processes. EDS/EDX analysis revealed that the outermost surface layer consisted of a thin layer of zinc oxide (ZnO), which exhibited extensive cracking and was also covered by various types of corrosion products, likely resulting from H₂S and CO₂ corrosion as shown in Fig. 4(a). Brittle transverse cracks of surface deposits along the length of the failed steel wires are observed, propagating from fracture locations as shown in Fig. 4(b).

The elemental composition analysis of three different fractured steel cords was carried out using EDS analysis of which the results are presented in Table 1. The results confirmed the presence of iron and zinc, consistent with initial galvanized zinc-coated carbon steel wires. The analysis of the multi-layer corrosion product in Fig. 4(a) indicated a composition richer in oxygen, while the surface layer over the carbon steel wires was richer in zinc, as evident from Sample 4 in Table 1. Sulfur-containing compounds were found on all analyzed fracture surfaces, indicating significant exposure to H₂S prior to the failure event. Brittle fracture surfaces exhibited notably higher amounts of sulfur compared to ductile fracture surfaces, highlighting the significant contribution of H₂S to the embrittlement. Sulfur-containing compounds were also detected on the wire cord surfaces, with the highest amount observed in the multi-layered product. Small amounts of chlorides were detected, consistent with the presence of produced water as the internal

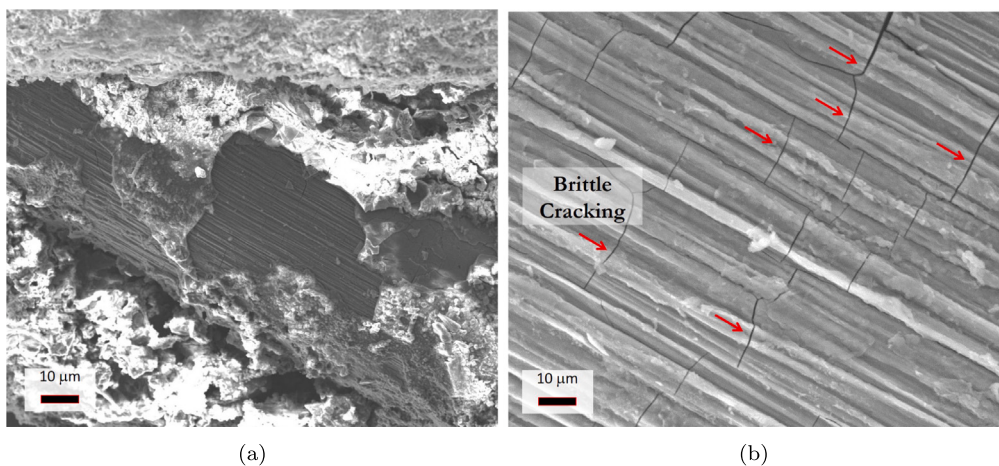


Fig. 4. SEM image of (a) multilayered corrosion products on a steel wire surface and (b) brittle cracking of a surface deposit on a steel wire.

Table 1

Elemental composition at different fracture surface locations measured in atomic percent (at. %).

Element	Steel Cord 1		Steel Cord 2		Steel Cord 3		Sample 4	Sample 5
	Ductile	Brittle	Ductile	Brittle	Ductile	Brittle		
O	2.70	7.64	1.64	12.61	–	31.48	32.66	3.58
Na	0.57	–	–	–	–	–	–	–
Mg	–	–	–	–	–	1.55	0.40	–
Al	0.21	–	–	0.17	0.15	–	0.38	0.77
Si	0.31	0.21	0.21	0.24	0.19	0.57	0.29	0.13
P	–	0.24	0.10	0.10	–	0.29	0.06	0.17
S	0.84	4.96	1.20	5.55	0.26	6.74	9.52	0.39
Cl	0.05	0.11	0.04	0.15	–	–	–	–
K	–	–	–	0.16	–	0.10	0.66	–
Ca	0.16	0.12	0.04	0.46	0.10	4.34	–	–
Mn	0.52	0.50	0.55	0.26	0.51	0.17	–	–
Fe	86.07	60.40	87.03	45.19	92.12	35.05	15.32	29.78
Ni	–	–	–	–	0.33	0.19	0.36	0.37
Zn	0.67	17.74	1.45	1.78	0.68	5.14	26.15	54.09

medium in the pipe. Other elements detected, such as oxygen, manganese, and nickel, can be attributed to corrosion and alloying components of the carbon steel cord wires.

4.4. Hardness testing

Hardness testing of the wire cross-sections was conducted to evaluate the mechanical properties of the wire cords. Using the Vickers hardness scale (HV), multiple measurements were taken on the metallographic cross-sections to determine the average hardness. The results revealed an average hardness of 55 to 56 HRC, consistent with the characteristic hardness range of AISI 1020 cold-drawn carbon steel wires. This hardness level is severely susceptible to sulfide stress cracking when subjected to wet H₂S and stress.

To assess the mechanical properties of the HDPE components in the failed pipeline, Shore hardness testing was performed on the outer jacket and inner liner. The measurements indicate that both the inner HDPE liner and the outer HDPE jacket fell within the typical hardness range for HDPE, ranging from 55 to 70 Shore D. Therefore, it can be concluded that the mechanical properties of the HDPE components were within acceptable limits and likely did not contribute to the failure.

5. Finite element modeling

In order to understand the complex mechanics of the RTP, the interaction of its various parts and how they relate to the observed failure, a finite element modeling approach is developed. Simulating the full RTP with all its details, especially considering its intricate braided steel wires and cords, presents computational challenges due to the numerous internal components, as illustrated in Fig. 1. To address this, a two-level FEM approach was adopted. In the first stage, a meso-scale model is created to capture the effective behavior of the steel cords, consisting of an assembly of braided steel wires. A simulated tensile test of this assembly is

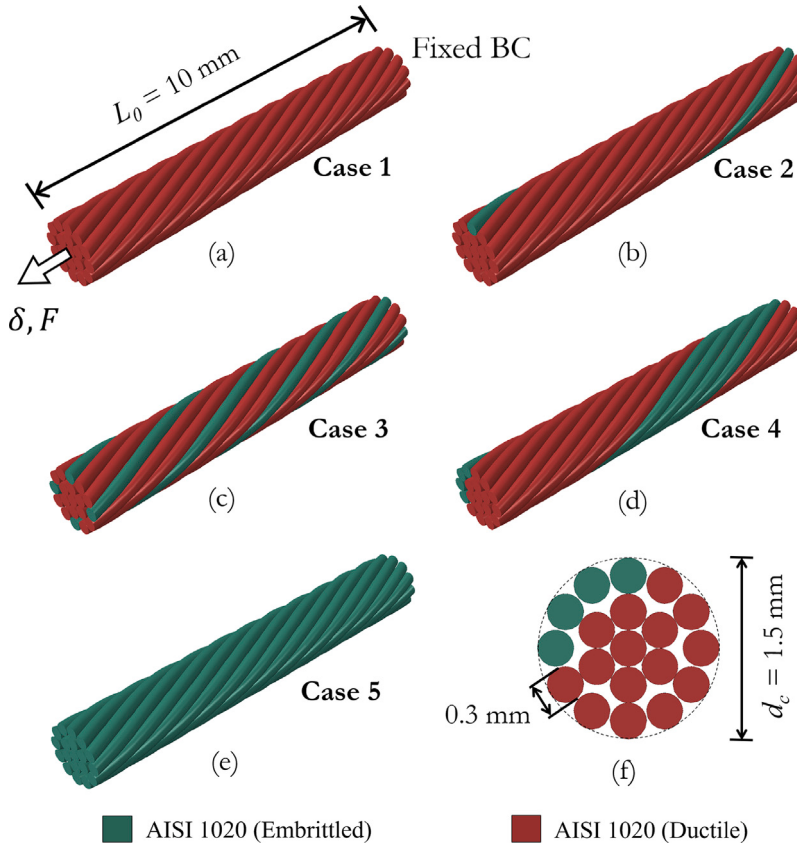


Fig. 5. Modeling scenarios of (a) fully ductile cord (Case 1), (b) cord with one embrittled wire (Case 2), (c) cord with four non-adjacent embrittled wires (Case 3), (d) cord with four adjacent embrittled wires (Case 4), (e) fully embrittled cord (Case 5), and (f) cross-section of Case 4 cord as an example with its 19 wires.

conducted to derive the effective stress-strain relationship of one cord. With the effective stress-strain data from the meso-scale model, the entire RTP, including the HDPE layers, was modeled in the second stage. To reduce computational cost, the assembly of wires in each braided steel cord was treated as a singular cord with an equivalent mechanical response derived from the meso-scale model results.

To evaluate the impact of hydrogen embrittlement on the RTP, two variations of the model were developed. One model incorporates the effect of hydrogen embrittlement on the steel wires, while the second does not. This differentiation is achieved in the meso-scale phase of the analysis. For the non-embrittled wires, AISI 1020 steel in as-installed conditions was utilized. The hydrogen embrittlement effect, however, is specifically incorporated by considering the mechanical response of embrittled AISI 1020 steel. This approach ensures that the broader RTP simulations reflect both conditions with precision, enabling detailed insights into the RTPs overall mechanical response.

5.1. Braided steel cord model (stage 1)

In this stage the effect of several physical variables on the mechanical response of the steel cord assembly is explored. First, the effect of frictional interaction between the steel cord wires on the effective uniaxial mechanical response of the steel cord assembly is investigated, assuming no hydrogen embrittlement. The friction coefficient μ is here varied in from frictionless to rather high the frictional contact interaction, e.g. $\mu = 0.0, 0.1$, and 0.3 . Another important aspect in this stage of modeling is evaluating the effect of number of embrittled wires in the cord on the effective uniaxial mechanical response, especially as it is evident from the SEM examination in Fig. 3 that embrittlement of these steel cord wires is prominent due to the H_2S exposure. As shown in Fig. 5, five different cases are considered here pertaining to a cord with fully ductile AISI 1020 steel wires (Case 1), a cord with one embrittled wire (Case 2), a cord with four non-adjacent embrittled wires (Case 3), a cord with four adjacent embrittled wires (Case 4) and a cord with fully embrittled wires. Here Case 4 pertains to the scenario depicted in the SEM fractographs shown in Fig. 3(a), which reveals the presence of embrittled wires.

A three-dimensional non-linear finite element model assuming quasi-static loading developed in Abaqus/Explicit to model the braided steel cord and its wires, as shown Fig. 5. The steel cord assembly was modeled with a total length of 10 mm, with the first layer consisting of 6 wires helical coiled in a clock-wise direction around the inner core wire, while the second layer comprises of 12 wires helical coiled in a counter-clockwise direction [39].

Table 2

Material parameters for ductile and embrittled AISI 1020 steel.

AISI 1020	E (GPa)	σ_y (MPa)	σ_{ut} (MPa)	ϵ_0	ϵ_s	ϵ_N	N	m_2	α_{sl}
Ductile	210	310	522	0.023	0.0100	0.0095	0.233	0.102	0.656
Embrittled	210	310	475	0.023	0.0163	0.0160	0.254	0.102	0.292

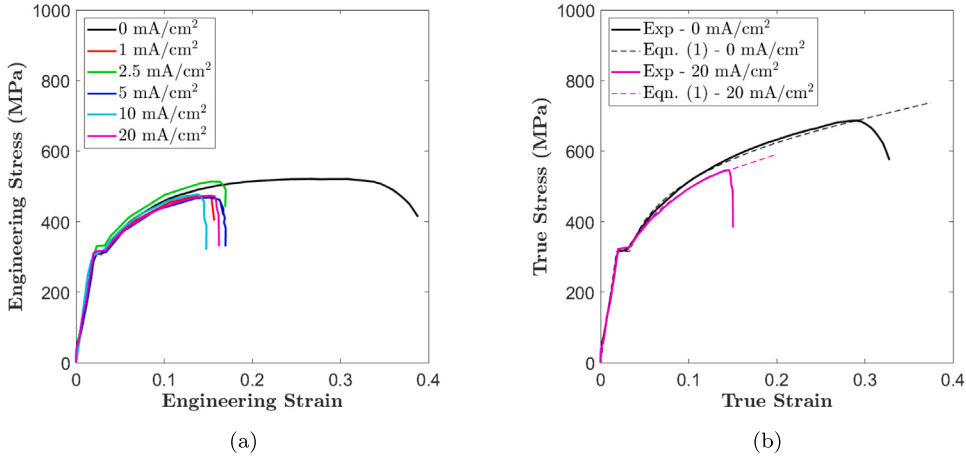


Fig. 6. (a) Engineering stress–strain curves of AISI 1020 under different hydrogen charging conditions (digitized from [43]), (b) true stress–strain curves of ductile ($0 \text{ mA}/\text{cm}^2$) and hydrogen embrittled ($20 \text{ mA}/\text{cm}^2$) AISI 1020 carbon steel.

5.1.1. Constitutive material behavior

Cai et al. [43] conducted uniaxial tensile tests to investigate hydrogen embrittlement characteristics of AISI 1020 cold-drawn carbon steel, which showed relatively high hydrogen embrittlement susceptibility as compared to other pipeline steels. By changing the current density of hydrogen charging, they investigated the effect of embrittlement on the stress–strain behavior, as shown in Fig. 6(a), where current density of $0 \text{ mA}/\text{cm}^2$ corresponds to the default uncharged case (e.g. ductile), and anything above zero charge correspond to embrittled AISI 1020 [43]. They noted that as current density increases, the level of hydrogen embrittlement is more severe, and the fracture mode of the steel transforms from ductile dimple rupture to brittle cleavage fracture, similar to as is observed in Fig. 3.

Hence, in the current study, we consider the $0 \text{ mA}/\text{cm}^2$ case as the reference stress–strain curve pertaining to AISI 1020 steel with fully ductile characteristics, whereas the case with $20 \text{ mA}/\text{cm}^2$ charge is adopted to represent the mechanical response of embrittled AISI 1020 steel. The true stress–strain curve of both ductile and embrittled AISI 1020 steel are fitted to an elastic–plastic model with isotropic hardening given by

$$\sigma = \begin{cases} E\epsilon & \epsilon < \epsilon_0 \\ \sigma_y & \epsilon_0 < \epsilon < \epsilon_s + \epsilon_N \\ \sigma_y \left(\frac{\epsilon - \epsilon_s}{\epsilon_N} \right)^N & \epsilon > \epsilon_s + \epsilon_N \end{cases} \quad (1)$$

where σ_y is the initial yield strength, ϵ_0 the initial yield strain, ϵ_N is a normalizing strain, ϵ_s is an offset strain, and N is the hardening exponent [44]. In the strain region $\epsilon_0 < \epsilon < \epsilon_s + \epsilon_N$, the stress is constant at σ_0 , pertaining to a Lüder plateau as evident in the tensile tests in Fig. 6. The parameters in Eq. (1) are provided for both the ductile reference case and the embrittled case of AISI 1020 in Table 2.

5.1.2. Material damage model

Damage state in the material was also modeled using a continuum damage mechanics approach. The damage behavior was represented by both damage initiation criterion and a damage evolution law, following the approach proposed in [44], which provides an enhancement of the ASME ductile failure criterion [45] incorporating the effect of stress state. The ASME criterion [45] inherently considers the concept of stress triaxiality T , given by

$$T = \frac{\sigma_h}{\sigma_e} \quad (2)$$

where σ_h and σ_e represent the hydrostatic and von-Mises equivalent stresses, respectively. The stress triaxiality level governs the microvoid growth and coalescence mechanisms in the ductile failure process [46,47]. However, as has been revealed through

experimental studies [44,48] that the stress state in a ductile solid is best characterized by both the stress triaxiality T and the Lode parameter L , which is defined as

$$L = \frac{2\sigma_2 - \sigma_1 - \sigma_3}{\sigma_1 - \sigma_3} \quad (3)$$

where $\sigma_1 \geq \sigma_2 \geq \sigma_3$ are the principal stresses. The Lode parameter ranges from $-1 \leq L \leq +1$, where $L = -1$ corresponds to the asymmetric tensile condition, $L = 0$ corresponds to the generalized shear or plane strain condition, and $L = +1$ corresponds to generalized compression or equibiaxial tensile condition. The ductile failure criterion proposed in [44,48] introduces an empirical Lode sensitivity parameter L_S given by

$$L_S = \begin{cases} 1 & \sigma_{ut} \leq \sigma_{ut}^{th} \\ -0.2208 \left(\frac{\sigma_{ut}}{\sigma_{ut}^{th}} \right)^2 + 1.7032 \left(\frac{\sigma_{ut}}{\sigma_{ut}^{th}} \right) - 0.4824 & \sigma_t > \sigma_{ut}^{th} \end{cases} \quad (4)$$

σ_{ut} represents the ultimate tensile strength, and σ_{ut}^{th} is the threshold value for ultimate tensile strength. Steels display Lode sensitivity in their ductile failure locus for $\sigma_{ut} > \sigma_{ut}^{th}$. Both the non-embrittled and embrittled AISI 1020 steel exceed the threshold limit of $\sigma_t^{th} = 450$ MPa, as shown in Table 2. Hence, the failure locus, e.g. limiting equivalent plastic failure strain ϵ_0^f , is given by

$$\epsilon_0^f = \epsilon_{Lu} \left[L^2 + \frac{(1-L^2)}{L_S} \right] \exp \left[- \left(\frac{\alpha_{sl}}{1+m_2} \right) \left(T - \frac{1}{3} \right) \right] \quad (5)$$

where ϵ_{Lu} is the uniaxial strain limit, m_2 is the strain hardening coefficient, and α_{sl} is a material constant dependent on the metallurgical structure. Values of m_2 and α_{sl} for both embrittled and non-embrittled AISI 1020 steel are obtained from the ASME Sec. 8, Div. 2 standard [45] and tabulated in Table 2. In this study, damage is considered to initiate when the plastic strain in any material point in the FE model reaches ϵ_0^f .

After damage initiation, for the case of ductile AISI 1020 steel (non-embrittled), the ductile damage evolution is modeled through a scalar damage approach, similar to [49–51], in which the experimental true stress–strain softening response ($\tilde{\sigma}$) of the material is related to the undamaged theoretical response (σ) through

$$\tilde{\sigma} = (1 - d_{mat})\sigma \quad (6)$$

where d_{mat} is the damage parameter ranging from zero at damage initiation, to one at complete stiffness loss at an equivalent plastic strain $\epsilon_f^p l$, as demonstrated in Fig. 7(a). Stiffness degradation is modeled through

$$E' = (1 - d_{mat})E \quad (7)$$

where E' is the degraded Young's modulus after damage initiation. The softening in the post-damage initiation stage and the evolution of the scalar damage parameter d_{mat} are characterized by a stress–displacement response [52] and require the introduction of a characteristic length l_e associated with a material point, which is computed automatically in the FEA model based on element geometry and size. The evolution of the damage parameter d_{mat} as function of plastic equivalent displacement u_{pl} measured over the gauge length l_g (i.e., $u_{pl} = \epsilon^{pl} l_g$) as shown in Fig. 7(b), is determined from the stress-strain values in the softening branch in Fig. 7(a). Hence, the plastic displacement at failure u_f^{pl} can be determine at $d_{mat} = 1$. A complete loss of load-carrying capacity in an element is achieved when the effective plastic displacement in the element, i.e., $u_{pl} = \epsilon^{pl} l_e$, reaches the u_f^{pl} where l_e is the characteristic length of the finite element [53]. When an element reaches its maximum load-carrying capacity, the element deletion method is utilized.

In the case of the embrittled AISI 1020, complete loss of load-carrying capacity in an element is achieved when damage initiation occurs. However, this would cause numerical instabilities due to the sharp change in the element stiffness upon reaching the initiation point; hence, a negligible linear damage evolution law was added to prevent possible numerical errors.

A mesh convergence study was performed to evaluate the impact of mesh density on the accuracy of the results, given the length scale dependency of the damage evolution model. The mesh sensitivity study was conducted such that one wire of the braided steel cord is stretched in a uni-axial tensile fashion, with a ductile (non-embrittled) AISI 1020 material model accounting for both damage initiation and evolution, for which the results are shown in Fig. 8(a). The findings show that an element size of 0.0225 mm offers a fair compromise between accuracy and computing time, and as a consequence, this size was chosen for subsequent analyses.

5.1.3. Effect of friction

Frictional contact interaction is assigned between the 19 wires of the steel cord, as depicted in Fig. 8(b). Results in Fig. 8(b) show that varying the friction coefficient does not have a significant effect on the mechanical response of the cord. Increasing the friction coefficient increases the failure displacement of the system by a small margin, with a minimal change in the maximum force that the structure can handle. As shown in the contact pressure contour in Fig. 9, pertaining to the center wire of the cord assembly, results reveal that the influence of friction is limited since contact interaction area is restricted to a line interaction between the wires.

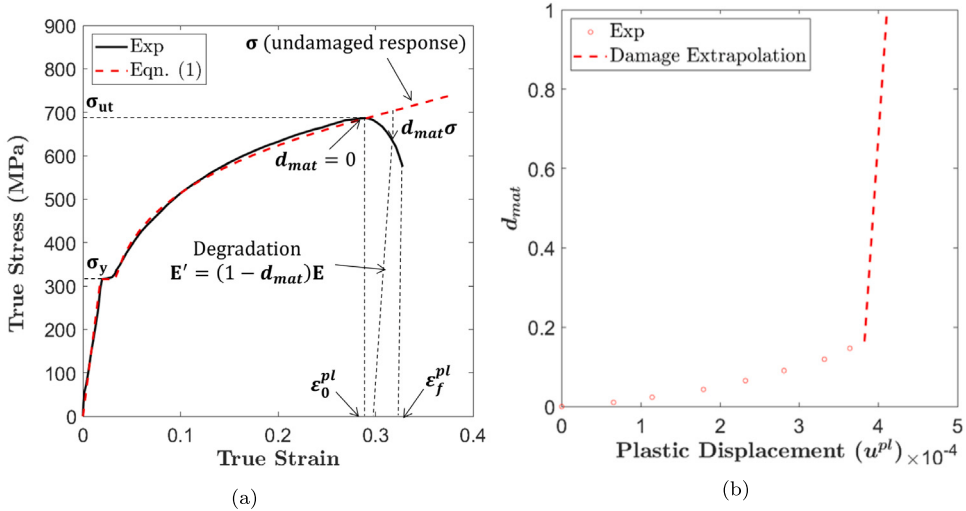


Fig. 7. (a) Schematic of the damage model and (b) damage evolution variable vs. plastic displacement for AISI 1020 steel under normal conditions.

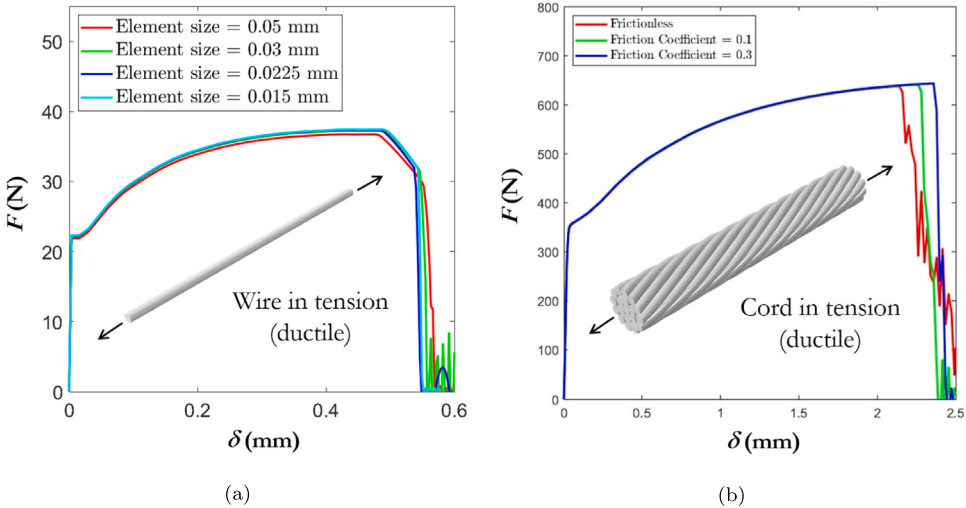


Fig. 8. (a) Mesh sensitivity analysis of a single wire under tension using the damage model, and (b) effect of friction coefficient on the force–displacement curve of the steel cord assembly, with element size of 0.0225 mm.

5.1.4. Effect of hydrogen embrittlement

The influence of hydrogen embrittlement on the braided steel cord assembly is detailed in this section, exploring various scenarios of embrittlement. Fig. 10(a) illustrates the force–displacement curves for the five different cases considered in Fig. 5. The results provide an understanding of how embrittlement alters the mechanical response of the cord, marking a critical transition from ductility to brittle behavior. When comparing the mechanical response of the fully ductile (Case 1) and fully embrittled (Case 5) cords in Fig. 10(a), there is a noticeable decrease in both the failure displacement (e.g. ductility) and the maximum load, reducing by approximately 45% and 12%, respectively. For the case with four embrittled wires (Case 3 and 4), the results reveal a two step reduction in the load-carrying capacity as shown in 10(b).

The force–displacement response and failure behavior of Case 4 in Fig. 10(b) and (c), with partially embrittled wires, reveals the complex interaction between the embrittled and non-embrittled wires in the cord assembly. The initial drop in force is attributed to the onset of failure of the embrittled wires in the cord at displacement $1.0 \leq \delta \leq 1.5$ mm. For displacements $1.5 < \delta < 2.0$ mm there is an insignificant change in force level during which the embrittled wires rupture. At complete rupture of the embrittled wires ($\delta \approx 2.0$ mm), the intact ductile wires start to carry the tensile load until complete loss of load carrying capacity is reached at $\delta > 2.0$ mm.

Fig. 11 offers a comparison between the SEM images of the failed cord and numerical simulations for Case 4. The failed wires from the numerical results in Fig. 11(b), aligns closely with the SEM images Fig. 11(a), verifying the accuracy of the modeling

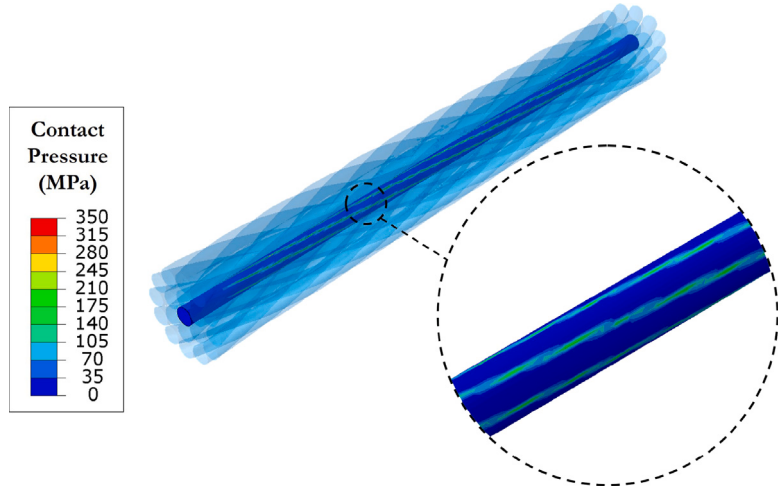


Fig. 9. Contact pressure contour of the cord assembly, emphasizing the center wire friction line-interactions with the surrounding wires assuming a friction coefficient of 0.3.

approaching utilized in capturing deformation and failure behavior under embrittled conditions. The von-Mises stress in Fig. 11(b) reveals that the stress at the instance of failure is higher in the ductile cord, corroborating its higher failure strength prior to damage initiation. The equivalent plastic strain (PEEQ) contours in Fig. 11(c) indicates that the ductile wires experience substantially higher deformation prior to failure, underlining the impact of reduced ductility due to hydrogen embrittlement. Overall, the excellent agreement between observation and the numerical results in Fig. 11 verifies the capability of the model in simulating the effect hydrogen embrittlement on the mechanical response of the cord assembly and provides hence a tool for exploring the failure of the full RTP.

5.2. Full RTP model (stage 2)

Utilizing the results from the meso-scale analysis in the previous stage and the mechanical response of the braided steel cords, this stage of the analysis seeks to analyze the failure behavior of the full RTP when embrittled and non-embrittled (e.g. ductile) steel cords are considered. Fig. 12 illustrates the structure of the RTP in the FE model, consisting of a pipe with outer diameter OD = 128 mm and a total length $L = 5 \times \text{OD} = 640$ mm. The models features three HDPE layers that encapsulate both steel reinforcement layers. Within the reinforcement layers, each steel cord is represented as a solid helical cylindrical wire of diameter $d_c = 1.5$ mm, with a total of 163 cords wound around the pipe at an helical angle of 45°. The thickness of the HDPE jacket cover layer, barrier layer and liner are $t_j = 1.5$ mm, $t_b = 1.0$ m and $t_l = 9.0$ mm, respectively.

5.2.1. Constitutive behavior of the RTP layers

The modeling of the full RTP requires detailed constitutive models for both the HDPE and reinforcement steel layers. For the steel reinforcement, two different constitutive material behaviors are considered in order to account for a non-embrittled (e.g. fully ductile) and partially embrittled conditions of steel cords. The engineering stress (σ_{eng}) and strain (ϵ_{eng}) are obtained from the non-embrittled (e.g. Case 1) and partially embrittled (e.g. Case 4) force-displacement response shown in Fig. 5. Assuming an equivalent circular cross-sectional area of the cord assembly, $\sigma_{\text{eng}} = F/A$ and $\epsilon_{\text{eng}} = \delta/L_0$, where F and δ are the axial force and displacement, respectively, $A = \pi d_c^2/4$ is the cross-sectional area with an equivalent cord diameter $d_c = 1.5$ mm, defined such that a cylindrical volume with length L_0 and diameter d_c is equal to the total volume of the cord assembly as shown in Fig. 5.

The true stress and strain are given by Eq. (8) and (9), respectively, and the corresponding equivalent true stress-strain curves for both the non-embrittled fully ductile (Case 1) and partially embrittled (Case 4) steel cord assemblies are illustrated in Fig. 13. Damage initiation is assumed to occur for both the non-embrittled and partially embrittled steel cord assemblies at the strain level of highest stress, as illustrated in Fig. 13. For the non-embrittled assembly, complete loss of load-carrying capacity in an element is achieved when damage initiation occurs. Hence, a negligible linear damage evolution law was added to prevent possible numerical errors and a linear stiffness degradation law is assumed to describe the degradation process, followed by element deletion to simulate the failure process.

$$\sigma_{\text{true}} = \sigma_{\text{eng}} \cdot (1 + \epsilon_{\text{eng}}) \quad (8)$$

$$\epsilon_{\text{true}} = \ln(1 + \epsilon_{\text{eng}}). \quad (9)$$

For the HDPE layers, an elastic perfectly-plastic constitutive behavior is adopted and the corresponding yield strength (21.8 MPa) and Young's modulus (829 MPa) at the working temperature of 35 °C are obtained from [54]. A damage behavior was assumed for

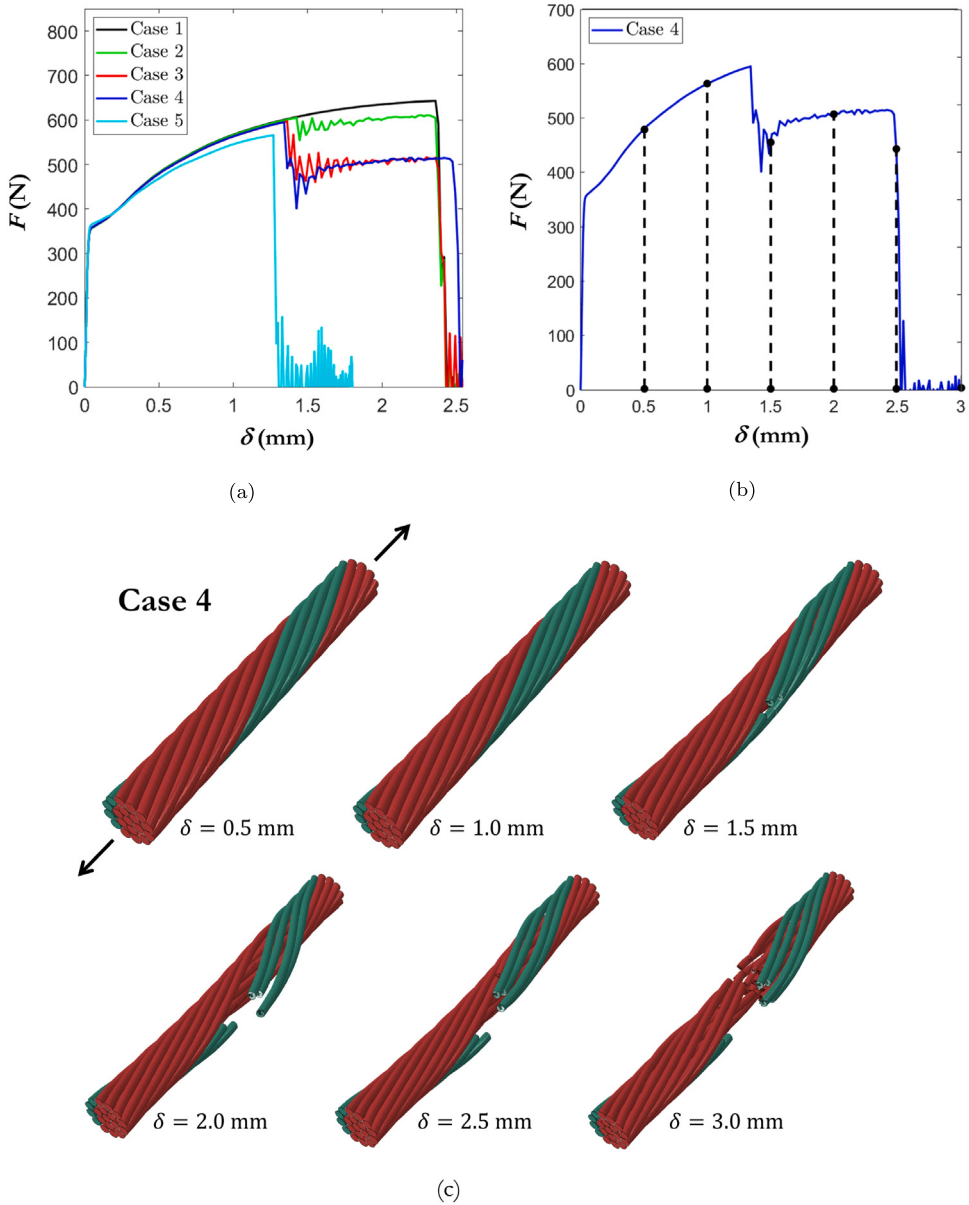


Fig. 10. (a) Force–displacement response for the five different cases considered ranging from fully ductile to fully embrittled steel cords assembly, (b) force–displacement for Case 4 with partially embrittled wires and (c) the failure of the cord wires at various displacements δ .

the HDPE layer, where failure is assumed to occur at a strain of 150%, using element deletion technique. This simplified approach of modeling the HDPE is justified as the HDPE layers are not the primary load-carrying components in the RTP assembly.

Both the equivalent steel cords and the HDPE layers are meshed with reduced integration linear hexahedral elements (C3D8R). The entire model is meshed with a total of 6,822,386 elements, as shown in Fig. 14, ensuring a detailed and accurate representation of the complex RTP structure. Both ends of the pipe are prescribed fixed displacement boundary conditions and an internal pressure is applied to the inner surface of the HDPE liner. Frictional contact interactions is prescribed such that a friction coefficient of 0.3 is used for steel-steel contacts and 0.17 for steel-HDPE contacts, as corroborated by previous research [55,56].

5.2.2. Burst pressure prediction

The RTP is subjected to an internal pressure P , as indicated in Fig. 12. As the steel cords in the reinforcement layer are the load carrying component in the RTP, failure is initiated and propagated in the steel cords, followed by failure in the external HDPE jacket, as shown in Fig. 14, which pertains to the case of partially embrittled cords. The burst pressure values obtained from the FEA results are given in Table 3 for the two RTP reinforcement layer conditions considered, e.g. non-embrittled (fully ductile) and

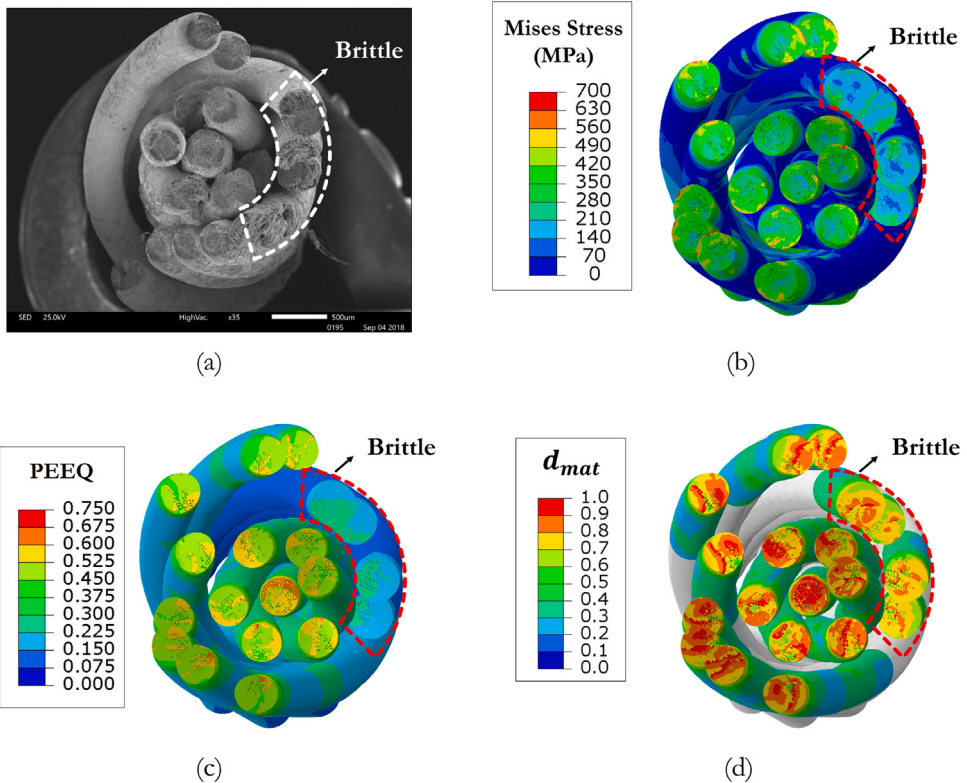


Fig. 11. Comparison of (a) an SEM image of one damaged cord against simulated (b) von-Mises stress, (c) equivalent plastic strain, and (d) d_{mat} parameter.

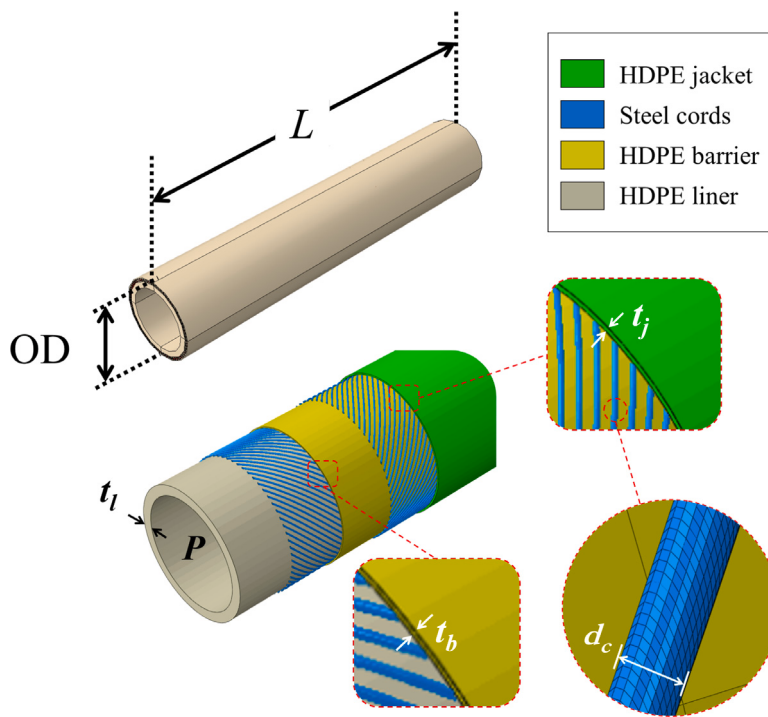


Fig. 12. The full RTP model with outer diameter $OD = 128$ mm, total length $L = 5 \times OD = 640$ mm, steel cord diameter $d_c = 1.5$ mm, jacket thickness $t_j = 1.5$ mm, barrier thickness $t_b = 1.0$ mm and liner thickness $t_l = 9.0$ mm.

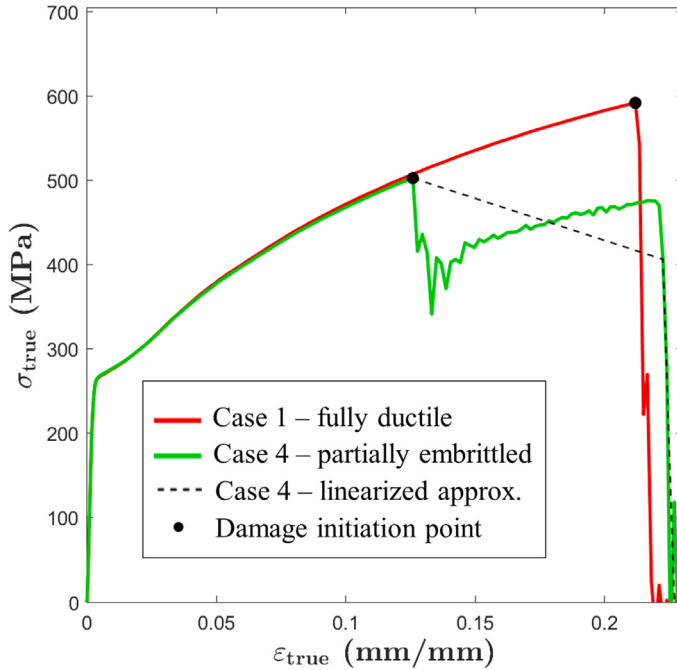


Fig. 13. Equivalent true stress–strain curves for unembrittled and partially embrittled steel cord assemblies, with the assumed damage model for the latter.

Table 3
Burst pressure predictions for different reinforcement layer conditions.

	P_f	Reinforcement (Cords)	Outer layer (HDPE)
Fully ductile	11.5 MPa		12.0 MPa
Partially embrittled	9.7 MPa		10.2 MPa

partially embrittled cords. These values delineate two separate failure mechanisms. One relating to failure of the reinforcement layer and its steel cords, and the other the HDPE layers. The burst pressure for the reinforcement layer is attained when the damage parameter reaches unity and the element is deleted subsequently from the steel cords in the model, signifying mechanical failure. Conversely, for the HDPE layers, burst pressure is attained when an element reaches a strain of 150% and is subsequently removed from the simulation. As shown in Table 3, the failure of the reinforcement layer consistently occurs before the failure of the HDPE layer. Consequently, the burst pressure of the RTP can be regarded as the minimum of these values, corresponding to the pressure at which the reinforcement layer fails.

The FEA results reveal that the burst pressure for the case of a fully ductile reinforcement layer is $P_f = 11.5$ MPa, while the burst pressure limit predicted for a partially embrittled reinforcement layer is $P_f = 9.7$ MPa. The latter agrees well with the internal pressure levels during operational conditions the RTP, ranging between 9.65 to 10.55 MPa. Hence, the hydrogen embrittlement of the steel cords in the reinforcement layer can be attributed to the primary cause of the reduction of the burst pressure capacity of the RTP and thus the root cause to the RTP failure, which is also endorsed by the experimental findings.

6. Conclusions

This study presents a comprehensive analysis of the failure of a reinforced thermoplastic pipe (RTP), which serves as a crucial component in the transportation of produced water from oil wells during the process of crude oil extraction. The study identified embrittlement of the steel cords of the reinforcement layer in the RTP, due to H₂S corrosion as a primary mechanism leading to the failure of the RTP, which is substantiated by electron dispersive spectroscopy (EDS) analysis and a thorough finite element analysis (FEA). Sulfur compounds on the wire surfaces, identified through EDS analysis, strongly support the assertion of embrittlement resulting from H₂S exposure. FEA results further confirmed this, revealing substantial reductions in ductility and strength of the reinforcement layer under embrittled conditions, highlighting the detrimental effects of the embrittlement due to H₂S exposure.

Moisture was detected in the annular space of the RTP prior to the failure event. While the exact source of this moisture remains uncertain, factors such as mishandling during installation or exposure to external environmental conditions were considered. FEA results demonstrated the significant impact of this moisture on the mechanical response of the cords and, consequently, the system's

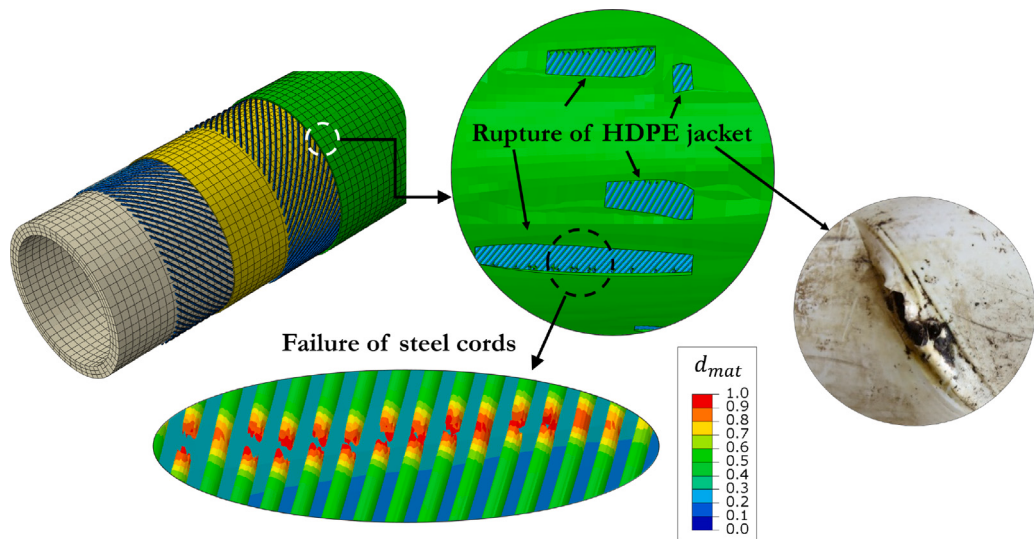


Fig. 14. Failure prediction in the RTP using embrittled cords, showing failure in the steel cords of the reinforcement layer and the outer HDPE layer. Case pertains to partially embrittled steel cords.

burst pressure. The findings also suggest that the carbon steel cords used in RTP construction are ill-suited for sour service conditions, as hardness measurements exceed the recommended levels for H₂S resistance limits.

FEA results further emphasized this vulnerability, particularly in the analysis of partially embrittled reinforcement layer, resulting in reduced burst pressure levels, closely agreeing with field observation. The accuracy of the FEA model in predicting the failure event was confirmed by its good agreement with scanning electron microscopy (SEM) findings at the meso-scale level and in predicting burst pressure level in the full RTP model. This validation enhances the confidence in the practical applicability of the developed FEA model for predicting and preventing failures in similar systems.

In summary, this study provides a comprehensive understanding of the multiple factors contributing to failure of RTPs subject to sour service environments, primarily focusing on their steel wire embrittlement due to H₂S exposure. To extend future work, we propose investigating hydrogen diffusion within the RTP material layers and incorporating fracture toughness degradation in a comprehensive diffusion-structural-damage numerical model. Such model would provide deeper understanding of the interplay between mechanical and environmental factors in hydrogen embrittlement, and can aid the design of RTPs for enhanced performance and structural integrity in challenging sour service conditions.

CRediT authorship contribution statement

M. Elkhodbia: Formal analysis, Investigation, Methodology, Validation, Writing – original draft, Writing – review & editing. **G. Mubarak:** Formal analysis, Investigation, Methodology, Validation, Visualization, Writing – original draft, Writing – review & editing. **I. Gadala:** Conceptualization, Data curation, Formal analysis, Investigation, Methodology, Project administration, Resources, Supervision, Validation, Visualization, Writing – original draft, Writing – review & editing. **I. Barsoum:** Conceptualization, Data curation, Formal analysis, Funding acquisition, Investigation, Methodology, Project administration, Resources, Software, Supervision, Validation, Visualization, Writing – original draft, Writing – review & editing. **A. AlFantazi:** Resources, Supervision, Writing – review & editing. **A. Al Tamimi:** Writing – review & editing.

Declaration of competing interest

The authors declare that they have no known competing financial interests or personal relationships that could have appeared to influence the work reported in this paper.

Data availability

Data will be made available on request.

Acknowledgments

The authors acknowledge the financial support provided by Abu Dhabi National Oil Company (ADNOC), United Arab Emirates under grant no. S.O. 9100000617/KUX 8434000453. The authors are thankful for the assistance of Mr. Wesley Latimer and Mr. Prakash Dodia at Acuren and SEMx Materials Analysis Laboratories in Calgary, Canada, with the experimental analyses.

References

- [1] L.T. Popoola, A.S. Grema, G.K. Latinwo, B. Gutti, A.S. Balogun, Corrosion problems during oil and gas production and its mitigation, *Int. J. Ind. Chem.* 4 (2013) 1–15.
- [2] A.O. Bukhari, M. Bashar, A.S. Aladawy, S.L. Goh, P. Sarmah, Review of non-metallic pipelines in oil & gas applications-challenges & way forward, in: International Petroleum Technology Conference, IPTC, 2022, D031S083R001.
- [3] Z. Wang, L. Zhang, T. Yu, M. Xu, Study of corrosion behavior of oil gathering facilities with CO₂ flooding in low-permeability oilfields, *Chem. Technol. Fuels Oils* 53 (2018) 933–942.
- [4] M. Askari, M. Aliofkhazraei, S. Ghaffari, A. Hajizadeh, Film former corrosion inhibitors for oil and gas pipelines-A technical review, *J. Nat. Gas Sci. Eng.* 58 (2018) 92–114.
- [5] Y.P. Asmara, The roles of H₂S gas in behavior of carbon steel corrosion in oil and gas environment: a review, *Jurnal Teknik Mesin (JTM)* 7 (1) (2018) 37–43.
- [6] M. Askari, M. Aliofkhazraei, S. Afroukhteh, A comprehensive review on internal corrosion and cracking of oil and gas pipelines, *J. Nat. Gas Sci. Eng.* 71 (2019) 102971.
- [7] M.E.A.B. Seghier, B. Kesh tegar, M. Taleb-Berrouane, R. Abbassi, N.-T. Trung, Advanced intelligence frameworks for predicting maximum pitting corrosion depth in oil and gas pipelines, *Process Saf. Environ. Protect.* 147 (2021) 818–833.
- [8] G. Mubarak, M. Elkhodbia, I. Gadala, A. Alfantazi, I. Barsoum, Failure analysis, corrosion rate prediction, and integrity assessment of J55 downhole tubing in ultra-deep gas and condensate well, *Eng. Fail. Anal.* (2023) 107381.
- [9] R.N. Burke, A.M.A. Al Tamimi, W.S. Al Shouly, D.E. Baetsen, Non-metallic technology deployment for the next generation of ADNOC production facilities, in: Abu Dhabi International Petroleum Exhibition and Conference, SPE, 2021, D021S062R001.
- [10] A. Tolmachev, S. Tolmacheva, Alternatives to steel pipes in the oil and gas industry, in: IOP Conference Series: Earth and Environmental Science, Vol. 459, (3) IOP Publishing, 2020, 032060.
- [11] C. Al Christopher, Í.G. da Silva, K.D. Pangilinan, Q. Chen, E.B. Caldona, R.C. Advincula, High performance polymers for oil and gas applications, *Reactive Funct. Polym.* 162 (2021) 104878.
- [12] F.G. Alabtah, E. Mahdi, F.F. Eliyan, The use of fiber reinforced polymeric composites in pipelines: A review, *Compos. Struct.* 276 (2021) 114595.
- [13] M. Lou, Y. Wang, B. Tong, S. Wang, Effect of temperature on tensile properties of reinforced thermoplastic pipes, *Compos. Struct.* 241 (2020) 112119.
- [14] M. Fahed, I. Barsoum, A. Alfantazi, M. Islam, Integrity assessment of internally corroded pipelines rehabilitated with a kevlar-reinforced flexible liner, *J. Press. Vessel Technol.* 142 (4) (2020) 041801.
- [15] Y. Wang, M. Lou, X. Zeng, W. Dong, S. Wang, Burst capacity of reinforced thermoplastic pipes based on progressive failure criterion, *Ocean Eng.* 234 (2021) 109001.
- [16] J. Shi, S. Zhong, X. Nie, J. Shi, J. Zheng, Study on steel wire reinforced thermoplastic pipes under combined internal pressure and bending moment at various temperatures, *Thin-Walled Struct.* 169 (2021) 108381.
- [17] J. Shi, Z. Hu, L. Zeng, P. Lu, H. Chen, N. Yu, X. Li, Study on mechanical failure behavior of steel-wire wound reinforced thermoplastic pipe under combined internal pressure and soil landslide conditions, *Materials* 16 (2) (2023) 848.
- [18] T. Cheldi, P. Cavassi, M. Serricchio, C.M. Spinelli, G. Vietina, S. Ballabio, Use of spoolable reinforced thermoplastic pipes for oil and water transportation, in: Offshore Mediterranean Conference and Exhibition, OMC, 2019, pp. OMC–2019.
- [19] L. Kong, H. Li, D. Qi, X. Li, Z. Yan, M. Xia, Q. Chen, F. Wang, X. Fan, Failure analysis of a reinforced thermoplastic pipe used in an oil transportation system, *Eng. Fail. Anal.* 138 (2022) 106403.
- [20] H. Teodorescu-Draghicescu, D. Scarlatescu, S. Vlase, M.L. Scutaru, C. Nastac, Advanced high-density polyethylene used in pipelines networks, *Procedia Manuf.* 22 (2018) 27–34.
- [21] R.J. Jiang, E. Slingerland, Y.F. Cheng, Corrosion of galvanised steel cord reinforcement in HDPE composite pipes in petroleum production, *Corros. Sci.* 49 (2013) 296–305. <http://dx.doi.org/10.1016/j.corsci.2010.12.018>.
- [22] L. Kong, X. Fan, N. Ding, H. Ding, X. Shao, H. Li, D. Qi, Q. Liu, Y. Xu, P. Ge, Experimental and simulation investigation on failure mechanism of a polyethylene elbow liner used in an oilfield environment, *J. Failure Anal. Prevention* 20 (2020) 2129–2136.
- [23] X. Zhang, L. Hou, H. Li, G. Qi, D. Qi, Leakage analysis of steel wire reinforced polyethylene composite pipe used for waste water transportation, *Eng. Fail. Anal.* 130 (2021) 105750.
- [24] L. Kong, H. Li, B. Wei, Z. Zhang, Cracking failure analysis of a steel wire-reinforced thermoplastic composite pipe used in an oily sewage conveying system, *J. Failure Anal. Prevention* 23 (1) (2023) 389–398.
- [25] H. Ding, A. Zhang, H. Li, D. Qi, G. Qi, N. Ding, Analysis of bulge failure of steel wire-reinforced thermoplastic composite pipe, *Eng. Fail. Anal.* 148 (2023) 107232.
- [26] S. Rehab-Bekkouche, W. Ghabeche, M. Kaddeche, N. Kiass, K. Chaoui, Mechanical behaviour of machined polyethylene filaments subjected to aggressive chemical environments, *Mechanics* 77 (3) (2009) 40–46.
- [27] R. Jiang, E. Slingerland, Y. Cheng, Corrosion of galvanised steel cord reinforcement in HDPE composite pipes in petroleum production, *Corrosion Eng., Sci. Technol.* 49 (4) (2014) 296–302.
- [28] H. Li, X. Zhang, H. Chu, G. Qi, H. Ding, X. Gao, J. Meng, Molecular simulation on permeation behavior of CH₄/CO₂/H₂S mixture gas in PVDF at service conditions, *Polymers* 14 (3) (2022) 545.
- [29] F. Sarrasin, P. Memari, M.-H. Klopffer, V. Lachet, C.T. Condat, B. Rousseau, E. Espuche, Influence of high pressures on CH₄, CO₂ and H₂S solubility in polyethylene: Experimental and molecular simulation approaches for pure gas and gas mixtures. Modelling of the sorption isotherms, *J. Membr. Sci.* 490 (2015) 380–388.
- [30] H.U. Khalid, M.C. Ismail, N. Nosbi, Permeation damage of polymer liner in oil and gas pipelines: A review, *Polymers* 12 (10) (2020) 2307.
- [31] M. Elkhodbia, A. Negi, G. Mubarak, I. Barsoum, A. Alfantazi, Review on sulfide stress cracking in sour service for OCTG and recent advances in modeling of hydrogen-assisted fracture, *Geoenergy Sci. Eng.* (2023) 212174.
- [32] Y. Bai, W. Chen, H. Xiong, H. Qiao, H. Yan, Analysis of steel strip reinforced thermoplastic pipe under internal pressure, *Ships Offshore Struct.* 11 (7) (2016) 766–773.
- [33] P. Shang, A. Xu, J. Zhao, Mechanical property analysis of two kinds of steel wire reinforced composite pipes, *J. Intell. Eng. Stems* 5 (3) (2012) 11–18.
- [34] H. Lu, M.A. Vaz, M. Caire, Alternative analytical and finite element models for unbonded flexible pipes under axisymmetric loads, *Ocean Eng.* 225 (2021) 108766.
- [35] H. Lu, M.A. Vaz, M. Caire, A finite element model for unbonded flexible pipe under combined axisymmetric and bending loads, *Mar. Struct.* 74 (2020) 102826.
- [36] H. Xiong, Y. Bai, H. Qiao, W. Ruan, Analysis on the mechanical properties of the plastic pipe reinforced by cross helically winding steel wires (PSP) under internal pressure, in: International Conference on Offshore Mechanics and Arctic Engineering, Vol. 56512, American Society of Mechanical Engineers, 2015, V05AT04A042.
- [37] J. Shi, J. Rao, X. Li, S. Shen, Y. Shen, A review of design, manufacture, and mechanical properties of steel skeleton reinforced thermoplastic pipes, *J. Pipeline Syst. Eng. Practice* 14 (4) (2023) 03123002.

- [38] J. Shi, J. Shi, H. Chen, Y. He, Q. Wang, Y. Zhang, G. Li, Short-term mechanical analysis of polyethylene pipe reinforced by winding steel wires using steel wire spiral structural model, *J. Press. Vessel Technol.* 140 (3) (2018) 031404.
- [39] Shawcor Composite Systems - Composite Linepipe, <https://www.shawcor.com/composite-systems/composite-linepipe>.
- [40] ASTM A370 Standard Test Methods and Definitions for Mechanical Testing of Steel Products, ASTM International, 2023, URL <https://www.astm.org/Standards/A370.htm>.
- [41] ASTM D 2240 Standard Test Method for Rubber Property—Durometer Hardness, ASTM International, 2021, URL <https://www.astm.org/Standards/D2240.htm>.
- [42] D. Qi, J. Ren, H. Li, P. Ren, H. Zhang, The permeation law of hydrogen sulfide in multilayer polymer composite oil/gas pipes, *Nat. Gas Ind.* 34 (2014) 126–130, <http://dx.doi.org/10.3787/j.issn.1000-0976.2014.05.018>.
- [43] L. Cai, G. Bai, X. Gao, Y. Li, Y. Hou, Experimental investigation on the hydrogen embrittlement characteristics and mechanism of natural gas-hydrogen transportation pipeline steels, *Mater. Res. Express* 9 (4) (2022) 046512.
- [44] N. Baghous, I. Barsoum, Effect of material strength on ductile failure of steel in pressure vessel design, *J. Press. Vessel Technol.* 143 (2) (2021) 021503.
- [45] ASME-BPVC, Section VIII, Div. 2, Rules for Construction of Pressure Vessels: Division 2-Alternative Rules, ASME, 2021, p. 872.
- [46] F.A. McClintock, A criterion for ductile fracture by the growth of holes, *J. Appl. Mech.* 35 (2) (1968) 363–371.
- [47] J.R. Rice, D.M. Tracey, On the ductile enlargement of voids in triaxial stress fields, *J. Mech. Phys. Solids* 17 (3) (1969) 201–217.
- [48] I. Barsoum, M. Al-Khaled, The sensitivity to the lode parameter in ductile failure of tubular steel grades, *J. Press. Vessel Technol.* 140 (3) (2018) 031402.
- [49] A. Lundkvist, I. Barsoum, Z. Barsoum, M. Khurshid, Geometric and material modelling aspects for strength prediction of riveted joints, *Metals* 13 (3) (2023) 500.
- [50] I. Barsoum, F. Khan, A. Molki, A. Seibi, Modeling of ductile crack propagation in expanded thin-walled 6063-T5 aluminum tubes, *Int. J. Mech. Sci.* 80 (2014) 160–168.
- [51] M. Khurshid, Z. Barsoum, I. Barsoum, Load carrying capacities of butt welded joints in high strength steels, *J. Eng. Mater. Technol.* 137 (4) (2015) 041003.
- [52] A. Hillerborg, M. Modéer, P.-E. Petersson, Analysis of crack formation and crack growth in concrete by means of fracture mechanics and finite elements, *Cem. Concr. Res.* 6 (6) (1976) 773–781.
- [53] Dassault Systèmes, SIMULIA user manual, 2020.
- [54] A. Shahin, I. Barsoum, M. Islam, Constitutive model calibration of the time and temperature-dependent behavior of high density polyethylene, *Polym. Test.* 91 (2020) 106800.
- [55] M.E. Kinsella, B. Lilly, B.E. Gardner, N.J. Jacobs, Experimental determination of friction coefficients between thermoplastics and rapid tooling injection mold materials, *Rapid Prototyp. J.* 11 (3) (2005) 167–173.
- [56] S. Dhouibi, M. Boujelbene, M. Kharrat, M. Dammak, A. Maalej, Friction behavior of high density polyethylene (HDPE) against 304L steel: An experimental investigation of the effects of sliding direction, sliding history and sliding speed, *J. Surf. Interfaces Mater.* 1 (1) (2013) 71–76.